Journal of Applied Polymer Science

Preparation of a hydrophobically enhanced antifouling isotactic polypropylene/silicone dioxide flat-sheet membrane via thermally induced phase separation for vacuum membrane distillation

Na Tang,[1,2] Huaiyuan Han,[1,2] Lina Yuan,[1,2] Lei Zhang,[1,2] Xuekui Wang,[1,2] Penggao Cheng[1,2]

[1]College of Marine Science and Engineering, Tianjin University of Science & Technology, Tianjin 300457, People's Republic of China

[2]Tianjin Key Laboratory of Marine Resources and Chemistry, Tianjin 300457, People's Republic of China

Correspondence to: N. Tang (E-mail: tjtangna@tust.edu.cn)

ABSTRACT: Isotactic polypropylene (iPP) hydrophobic flat-sheet membranes were fabricated for use in vacuum membrane distillation (VMD) through a thermally induced phase-separation process with dispersing hydrophobically modified SiO_2 nanoparticles in the casting solution to achieve a higher hydrophobicity and to sustain a stable flux in VMD. The contact angle (CA) measurements indicated that the incorporation of nano-SiO_2 into a casting solution mixture containing 20 wt % iPP had a 20.9% higher CA relative to that of SiO_2-free membranes. The addition of nano-SiO_2 also induced morphological changes in the membrane structure, including changes in the pore size distribution, porosity, and suppression of macrovoids. The pore size distribution of the iPP–SiO_2 membranes became narrower compared with that of the SiO_2-free membranes, and the porosity also improved from 35.45 to 59.75% with SiO_2 addition. The average pore size and maximum pore size of the iPP–SiO_2 membranes both decreased. The ability of the membranes to concentrate an astragalus aqueous solution (a type of traditional Chinese medicine) with VMD was investigated. The surface hydrophobicity and antifouling performance of the iPP–SiO_2 membranes improved with nano-SiO_2 addition to the membrane casting solution. © 2015 Wiley Periodicals, Inc. J. Appl. Polym. Sci. **2015**, *132*, 42615.

KEYWORDS: membranes; nanoparticles; nanowires and nanocrystals; polyolefins; porous materials; properties and characterization

Received 2 December 2014; accepted 9 June 2015

DOI: 10.1002/app.42615

INTRODUCTION

Membrane distillation (MD) is a thermal membrane separation process driven by the vapor pressure difference across a hydrophobic porous membrane.[1–3] The advantages of MD processes include low-temperature and low-pressure operating conditions, reduced interaction between the membrane and the feed solution, and a small space requirement for the vapor.[4] Primarily, there are four modes of MD configurations. The first MD mode is driven by a temperature gradient difference between the hot brine side of the membrane and the cold permeate side of the membrane. This mode is called *direct-contact membrane distillation* (DCMD). In the second mode, a vacuum is applied to induce vapor transport from the hot brine side of the membrane to the permeate side of the membrane. Then, the water vapor is condensed in a separate condenser. This vacuum-driven process is called *vacuum membrane distillation* (VMD).[5] The other two configurations of the MD process are *air-gap membrane distillation* (AGMD) and *sweep-gas membrane distillation* (SGMD). In AGMD, an air/vapor layer is interposed between the membrane and the condensation surface.[6] SGMD consists of a gas that sweeps the distillate side of the membrane carrying the vaporous distillate away from the distillate side of the membrane pore, whereas the feed liquid solution is kept at a higher temperature than the gas temperature.[7] The membrane used in the MD process acts as a physical support to prevent the feed solution from permeating the membrane and allowing the vapor to cross the dry pores. So, the ideal MD membrane must be of good hydrophobicity, narrow pore distribution, high porosity, and good mechanical strength. Generally, the hydrophobic microporous membranes are made from polypropylene, polyethylene, polytetrafluoroethylene, and poly (vinylidene fluoride) (PVDF). All of these hydrophobic membrane materials can basically fulfill the requirement of hydrophobicity. Among these hydrophobic membranes, isotactic polypropylene (iPP) is an outstanding membrane material because of its low cost, good mechanical properties, high thermal stability, and excellent resistance to acids, alkalis, and organic solvents.[8,9]

However, the widespread use of MD technology is limited by its low energy-utilization rate,[4] low fluxes,[10] long-term stability,[11]

membrane fouling, and so on. The major issue that limits the widespread use of the membrane technology in MD is membrane fouling. One of the most reason causing membrane fouling is the irreversible deposition of organics in the feed solution on the hydrophobic membrane surface; this results in a huge water flux loss and solute selectivity changes with time.[12,13] Researchers have made some attempts to control fouling; these include feed pretreatment, hydraulic and chemical cleaning, increases in the feed rate, decreases in the roughness, and high hydrophobic membrane surface.[14] Lv *et al.*[15] concluded that increasing the membrane hydrophobicity is a more effective method for overcoming membrane fouling. A series of studies have focused on the preparation of hydrophobic membranes. Singh *et al.*[16] prepared highly hydrophobic PVDF–clay nanocomposite nanofiber membranes through the blend electrospinning method and tested their performance in DCMD. Matsuura *et al.*[17] prepared 11 polyethersulfone (PES) membranes by incorporating a newly synthesized surface-modifying macromolecule into PES via a phase-inversion technique. Wang *et al.*[18] blended inorganic LiCl with the soluble polymer poly(ethylene glycol) (PEG) 1500 as a nonsolvent additive to fabricate PVDF hydrophobic hollow-fiber membranes via a phase-inversion process to obtain a higher permeate flux (J_w) and better hydrophobicity membranes. However, most of the preparations include strict conditions, such as harsh chemical treatment, expensive modification materials, and complex processing methods and devices. Therefore, a simple method that does not suffer from a high cost and limitations in large-scale hydrophobic surface production should be widely promoted.

In this study, iPP hydrophobic flat-sheet membranes were prepared with hydrophobic SiO_2 nanoparticles at different weight fractions. The goal of the research was to prepare iPP–SiO_2 membranes via thermally induced phase separation (TIPS) through the introduction of a certain proportion of nano-SiO_2 to effectively improve the membrane performance. The surface chemical structure, hydrophobicity, and surface structure of the membranes were examined by X-ray photoelectron spectroscopy (XPS), contact angle (CA) measurement, and scanning electron microscopy (SEM) techniques, respectively. The effects of the nano-SiO_2 concentration in the casting solution on the morphology of the membrane were also investigated. The performances of the membranes in the VMD process before and after the incorporation of nano-SiO_2 into the membranes were investigated with the choice of a much more easily polluted solution than aqueous NaCl solution, an astragalus aqueous solution, as a model foulant. The major ingredient of the astragalus solution was astragalus polysaccharides. There are some important characteristics of astragalus polysaccharides, including thermal sensitivity and oxidation. The information gained from this study will contribute to the fundamental knowledge required to prepare polymeric porous membranes with higher hydrophobicities by TIPS in combination with inorganic particles.

EXPERIMENTAL

Materials

iPP was obtained from the North China Petroleum Bureau of the China Petrochemical Group (Renqiu, China). Soybean oil, which was used as the solvent, was purchased from Beihai COFCO Grain and Oil Industry Co., Ltd. (Tianjin, China). Hydrophobic SiO_2 nanoparticles were supplied by Changsha Jing Kang New Material Co., Ltd. (Changsha, China) with a CA of approximately 120°. The particle size range and specific surface area of the SiO_2 nanoparticles were 7–40 nm and 120 m^2/g, respectively. The *n*-hexane, which was used as the extractant in the polymer solution, was supplied by the Tianjin Guangfu Research Institute of Fine Chemical Engineering (Tianjin, China). The astragalus used in this study was purchased from Beijing Tongrentang Co., Ltd. The aqueous extract solution was produced at an extraction temperature of 70°C with three times the amount of water added to the raw astragalus materials in three rounds of extraction, each of which lasted for 120 min.

Table I. Compositions of the Dope Solutions for Flat-Sheet Membrane Preparation

Membrane	SiO_2/iPP	iPP (wt %)	Oil bean (wt %)
Ma	0 : 100	20	80
Mb	5 : 100	20	79
Mc	10 : 100	20	78
Md	15 : 100	20	77
Me	20 : 100	20	76

Membrane Preparation

The iPP–SiO_2 membranes were prepared by the TIPS method.[19–21] The compositions of the dope solutions corresponding to each of the membrane samples (Ma, Mb, Mc, Md, and Me) are presented in Table I. The variable in the dope solution was the SiO_2 mass fraction in the iPP–SiO_2 blend. In brief, the iPP and SiO_2 nanoparticles were dissolved in soybean oil and dispersed homogeneously by an ultrasonic dispersion instrument. After that, the cast solution was stirred at 200°C for approximately 4 h to achieve a homogeneous mixture and then left for 8 h to allow the complete release of air bubbles. Next, the homogeneous dope solution was fed into the DKN-40 flat membrane casting equipment (pH-554 nonwoven fabric as the support layer) at a speed of 1.8 m/min. The thickness of the membranes was controlled to 0.28 mm. Then, the hot membrane was immersed in a coagulation bath of 20°C water to induce complete phase separation and to solidify the membrane. Subsequently, the pristine membrane was immersed in *n*-hexane for 24 h to completely remove the residual solvent, and then, the as-prepared membranes were dried in air at room temperature.

Membrane Characterization

Phase Diagram. The sample was placed between a pair of microscope cover slips. A Teflon film 100 μm in thickness with a square opening was inserted between the cover slips. The sample was heated on a hot stage at 200°C for 5 min and cooled to 20°C at a controlled rate of 10°C/min. We determined the cloud points visually by noting the appearance of turbidity under an optical microscope using an X-4 digital display micromelting point determination apparatus.

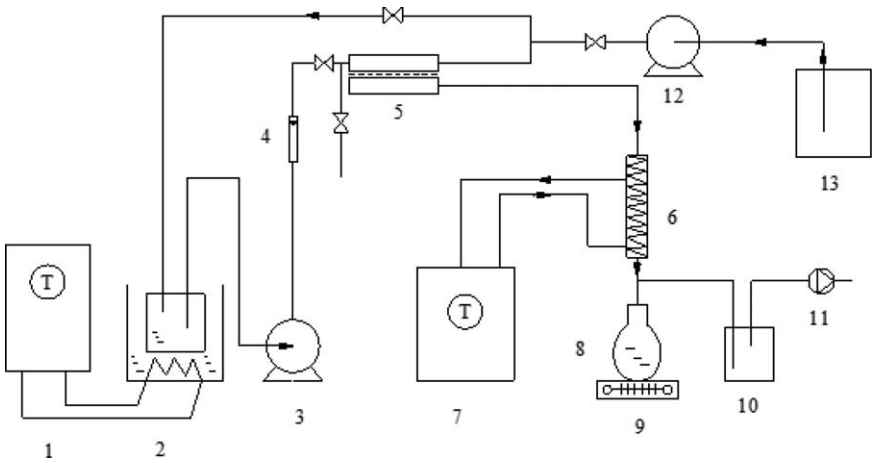

Figure 1. Schematic view of the VMD setup: (1) temperature controller, (2) feed tank, (3,12) pump, (4) rotameter, (5) flat-sheet membrane module, (6) condenser, (7) chiller, (8) distillate collector, (9) electronic balance, (10) buffer bottle, (11) water power vacuum pump, and (13) backwashing tank.

Differential scanning calorimetry (DSC; DSC 200F3, Netzsch Thermal Analysis, Germany) was used to determine the dynamic crystallization temperature (t_p) during the constant cooling period. An amount of 10 mg of the solid sample was sealed in an aluminum DSC pan, melted at 200°C for 5 min, and then cooled at a rate of 10°C/min to 25°C. The temperature at the onset of the exothermic peak during cooling was considered to be the crystallization temperature.[22]

For a nonisothermal crystallization process, the crystallization time (t) and temperature (T) are related as follows:

$$t = \frac{|T_0 - T|}{\beta_0} \tag{1}$$

where T_0 is the initial temperature when crystallization starts. β_0 is cooling rate, °C/min. Thus, the relative crystallinity as a function of temperature (X_t) is defined as follows:

$$X_t = \frac{\int_0^t (dH_c/dt)dt}{\int_0^\infty (dH_c/dt)dt} \tag{2}$$

where H_c is crystallization enthalpy, J/g.

SEM. Samples of the membranes were prepared by coating with a thin layer of Au via sputtering. The morphology of the cross sections and the surfaces of the membranes were examined with an SEM instrument (Hitachi SU1510, Hitachi, Ltd., Japan).

CA Measurement. The CA of the membranes was determined with a Kruss optical CA measuring instrument DSA100 (Germany). A droplet of water was formed on the flat surface of the membrane with a syringe, the CA of which was captured by a high-speed camera. The average of at least five measurements is reported.

Surface Morphology of the Membranes. Atomic force microscopy (AFM; JSPM-5200, JEOL Electronics Corp., Japan) was used to analyze the surface morphology of the prepared membranes. For comparison, the same tip was used to produce AFM images of the membranes, and all of the captured surfaces were treated in the same manner. The mean roughness (R_a) represents the mean value of the surface relative to the center plane, for which the volumes enclosed by the images above and below this plane are equal. The root mean square roughness (R_q) is the standard deviation of the Z axle within the specific area. R_a and R_q were calculated from the roughness profile determined by AFM.

Porosity, Pore Size, and Pore Size Distribution. The membrane porosity (ε) is defined as the pore volume divided by the total volume of the porous membrane. ε can be determined with the gravimetric method:[23]

$$\varepsilon\ (\%) = \left(1 - \frac{\rho_f}{\rho_p}\right) \times 100 \tag{3}$$

where ρ_f is the membrane apparent density (kg/m^3) determined by the gravimetric method and ρ_p is the polymer density (kg/m^3).

The pore size and pore size distribution of the prepared membranes were investigated with a capillary flow porimeter (Porolux 100, Germany). The fibers were fully wetted with Porefil. The pore size and pore size distribution were determined with the aid of the computer software Labview.

XPS. XPS was performed with a VG Scientific surface analysis system (United Kingdom). Soft X-rays were irradiated onto the sample to eject electrons from the core energy levels of the atoms. The electrons with low characteristic energies within the top few atomic layers of the surface escaped into the high-vacuum spectrometer and were analyzed to generate a photoelectron spectrum. The detailed peak shapes provided precise chemical specification, and the peak energy position provided the elemental analysis.

VMD Experiment

VMD Test. The VMD process was used to test the membrane performance. The simplified scheme of the VMD setup is shown in Figure 1. The effective membrane area was 28 cm^2.The feed was fed by a pump to the membrane module, with the flow rate controlled by a rotameter. When the feed was heated to the desired temperature, a waterpower vacuum pump was

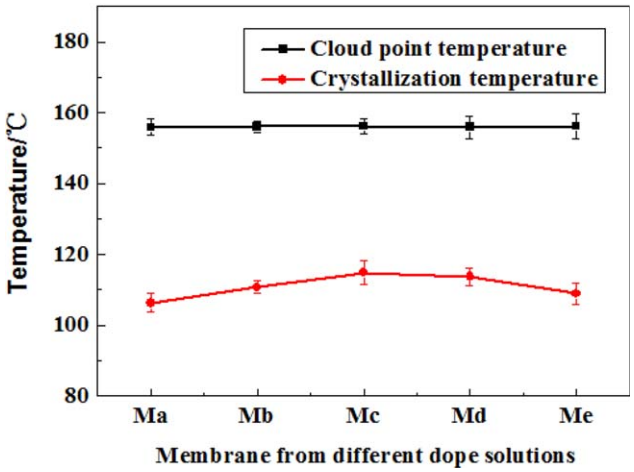

Figure 2. L–L separation and crystallization behavior for different membranes. [Color figure can be viewed in the online issue, which is available at wileyonlinelibrary.com.]

used on the permeate side to transfer the vapor through the membrane pores to the permeate side, where the vapor was condensed in the distillate collector. After 5 h of VMD operation time, the VMD process was stopped, and the backwashing process was initiated to clean the membrane with potassium permanganate as the cleaning agent. The cleaning conditions were as follows: the concentration of the cleaning agent was 2 g/L, the cleaning temperature was 30°C, and the cleaning time was 30 min.

The astragalus extract aqueous solution was used as the feed solution at a temperature of 343.16 K, the permeate temperature was maintained at 270 K, the absolute pressure at the permeate side was 0.095 MPa, and the feed recirculation rate was kept at 50 L/h.

J_w was calculated with the following equation:

$$J_w = \frac{\Delta w}{A \cdot \Delta t} \tag{4}$$

where J_w is the permeate flux (kg m^{-2} h), Δw is the mass of the permeate (kg), A is the effective surface area of the membranes (m^2), and Δt is the time interval (h).

The rejection rate (η) of the flat-sheet membranes was calculated according to the following equation:

$$\eta\ (\%) = \frac{C_f - C_p}{C_f} \tag{5}$$

where C_f is the concentration of the feed and C_p is the concentration of the permeate. C_f and C_p were calculated by the phenol–sulfuric acid method along with the use of a UV spectrophotometer (UV-3200PC, Shanghai Analytical Instrument, China) with polysaccharide as the parameter for water-extraction.

Membrane Antifouling Performances in VMD. In the membrane separation processes, *membrane fouling* refers to the deposition and accumulation of undesirable materials on the membrane surface and/or the membrane pores; this may reduce the process J_w and process efficiency.[3] The astragalus extract used in traditional Chinese medicine is a mixture with a complicated composition, including solid particles, tannic substances, proteins, macromolecules, gelatin, colloids, resin, and many other soluble ingredients.[24] Consequently, it is common to observe a flux decline during the process of concentrating astragalus extract by VMD.

RESULTS AND DISCUSSION

Phase Diagram Analysis

As shown in Figure 2, the liquid–liquid (L–L) phase-separation temperature (t_{cloud}) remained constant, whereas t_p increased with the addition of SiO_2 but decreased when the ratio exceeded 10 : 100 (Mc). This behavior was due to the iPP crystallization at a higher temperature, which was enabled by the addition of a certain amount of SiO_2, that is, through the reduction of the crystalline interface nucleation energy. The thermodynamic energy barrier of the nucleation process was lowered, and the nucleation capability of polymer particles was enhanced; however, the excessive addition of SiO_2 resulted in agglomeration and made the nucleation process more difficult. This thereby lowered the crystallization temperature.

The relative crystallinity as a function of time for the iPP and SiO_2/iPP nanoparticles is shown in Figure 3. The half-lifetime to reach 50% crystallinity was calculated for a cooling rate of 10°C/min, which was representative of the overall crystallization rate.

We observed that the order of crystallization rate was Mc < Mb < Me < Md < Ma. Mc exhibited the highest crystallization rate, whereas Ma (SiO_2-free membrane) exhibited the slowest rate. This was due to the more rapid crystallization of iPP in the presence of SiO_2, and it signified the nucleating effect of the silica nanoparticles. However, with increasing SiO_2 particle concentration in the SiO_2/iPP mixture, the SiO_2 nanoparticles acted as antinucleating agent and reduced the crystallization rate of the polymer.

Surface and Cross-Sectional Morphology Study

The SEM images of the Ma, Mb, Mc, Md, and Me membranes are presented in Figure. 4.

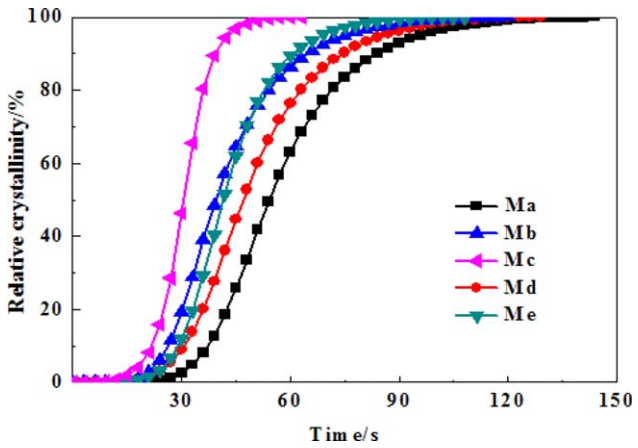

Figure 3. Relative crystallinity versus time for different dope solutions. [Color figure can be viewed in the online issue, which is available at wileyonlinelibrary.com.]

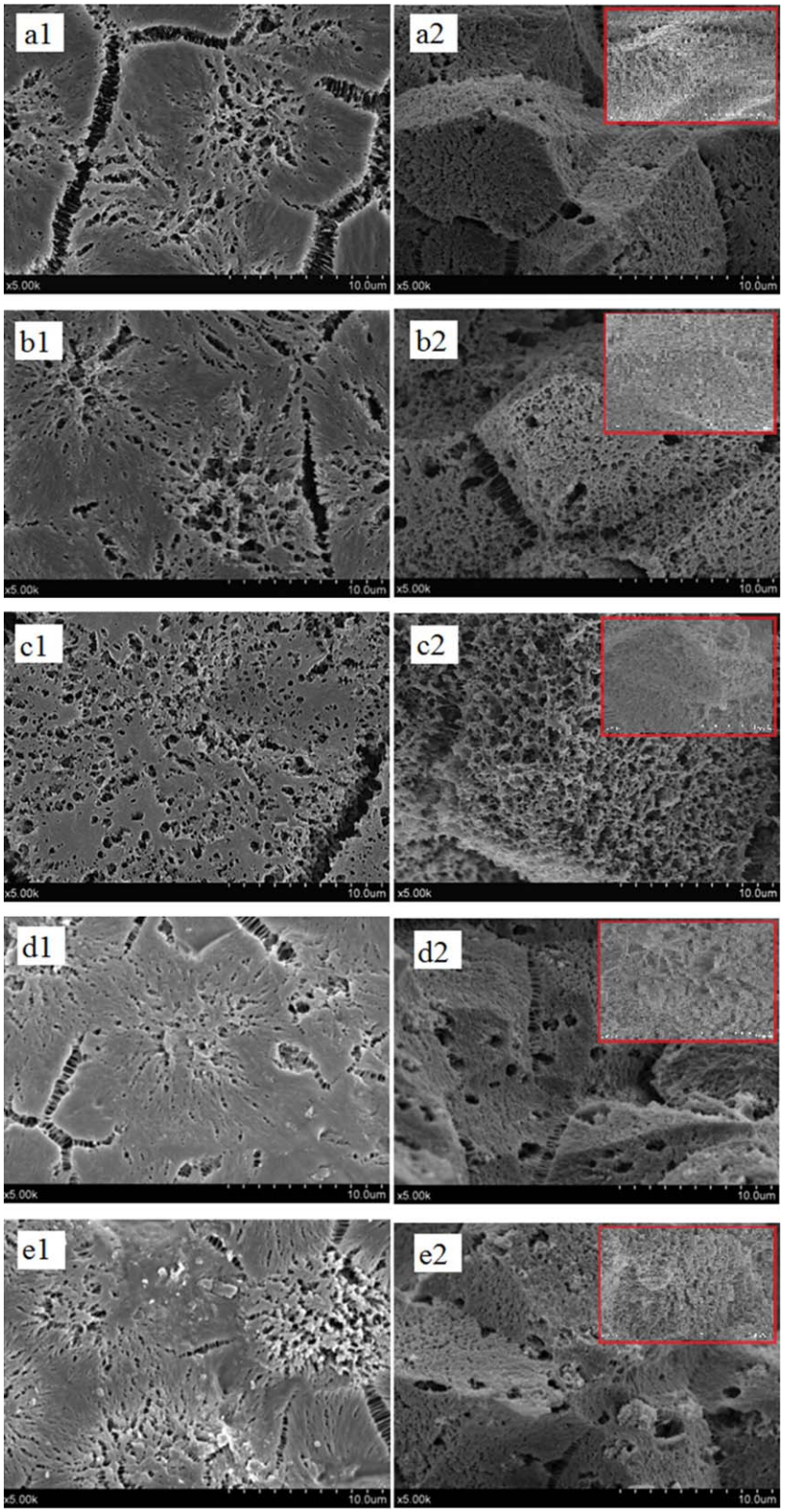

Figure 4. Top surface and cross-sectional morphology images of the iPP/SiO_2 membranes of (a) Ma, (b) Mb, (c) Mc, (d) Md, and (e) Me. (The top right corner images are a magnification of a part with 10,000× magnification.) [Color figure can be viewed in the online issue, which is available at wileyonlinelibrary.com.]

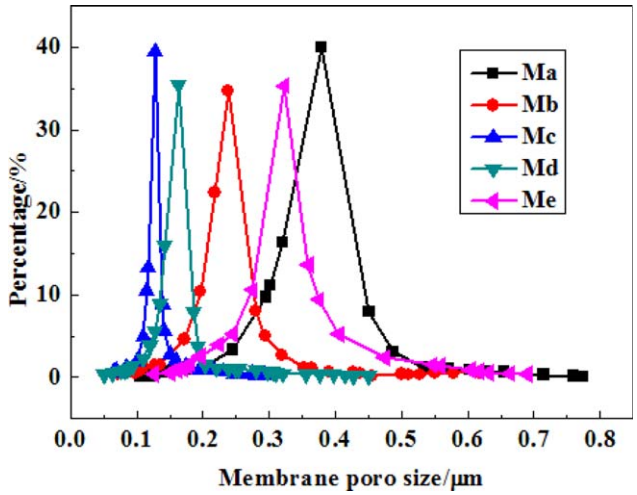

Figure 5. Pore size distribution of the membranes Ma, Mb, Mc, Md and Me. [Color figure can be viewed in the online issue, which is available at wileyonlinelibrary.com.]

We observed that the number of pores on the surface and cross section increased with the addition of nano-SiO_2 particles, and the porous layers became looser. We also observed that macrovoids decreased when the SiO_2/iPP was below 10 : 100. This observation could be explained by the process of membrane formation. During the phase-separation process, when the temperature of the solution was reduced to t_{cloud}, L–L phase separation occurred. Until the temperature of the solution reached t_p, solid–liquid (S–L) phase separation occurred according to a nucleation growth mechanism. So, t_{cloud}–t_p represented the L–L phase-separation process.[25] After the addition of SiO_2, the L–L t_{cloud} remained constant, whereas t_p increased when the SiO_2/iPP ratio was below 10 : 100. The process of L–L phase separation became shorter, whereas the crystallization rate increased. As a result, the coarsening time of the droplets decreased after the dilute solution was removed, and a smaller pore size formed.

The Mc membrane exhibited improved connectivity, as could be particularly observed from the cross-sectional image. This improved connectivity could be explained by the increase in the crystallization temperature of the membrane casting solution; this resulted in an increase in the dilute solution dispersal ability and an enhancement in the movement of the polymer chain. Thus, the poor phases of the polymer ran through mutually; this led to improved connectivity after the dilute solution was removed.

When the mixing ratio exceeded 10 : 100 (Me), ε began to decrease, and parts of the membrane pores were blocked by large particles. This behavior was related to the increase in the number of added particles, the aggregation of some of the nanoparticles in the prepared dope, and the nanoparticles acting as an antinucleation agent; this decreased the polymer crystallization rate and led to a slow L–L phase separation, which resulted in macrovoids.

Porosity, Pore Size, and Pore Size Distribution

The pore size distribution of the flat-sheet membranes are presented in Figure 5. For all of the iPP–SiO_2 membranes, the pore size distribution became narrower around the mean pore diameter compared with that of the pure iPP membrane and PVDF–TiO_2[26] and PVDF–SiO_2[27] hybrid membranes. The maximum pore size and mean pore diameter are listed in Table II. We found that when the addition of nanoparticles was lower than 10 : 100, the pore size of the iPP–SiO_2 membranes decreased with increasing amount of SiO_2; this was in agreement with the analysis of the membrane morphology. As shown in Table II, the reduction of the maximum pore size would be helpful in preventing solutions from passing through the membrane pores. Table II also shows the results of the porosity measurements among the samples with different SiO_2/iPP ratios. Although the porosity of the Md and Me membranes were 51.81 and 40.13%, respectively, that is, higher than the porosity of the pure iPP membrane, the porosity of the Md and Me membranes became lower compared with that of the Mc membrane. This indicated that the addition of nanoparticles was not always positive to ε. With increasing amount of SiO_2, the porosity increased first and then decreased. After the nano-SiO_2 particles were added, the crystallization temperature of the membrane casting solution increased; this resulted in an increase in the dilute solution dispersal ability and an enhancement of the diffusability of the dilute solution. Thus, this led to a higher porosity after the dilute solution was removed. However, when the SiO_2/iPP ratio exceeded 10 : 100, the agglomeration of the nanoparticles appeared, and some membrane pores were even blocked by large agglomerated particles. This resulted in a decrease in ε.

Confirmation of the Nanostructures of the Modified Membrane Surfaces

The surface morphology and three-dimensional topographical images of the membranes (i.e., top and bottom surfaces of the flat-sheet membranes) for the pure iPP membrane (Ma) and the SiO_2/iPP membrane (Me) are presented in Figure 6. All of the roughness parameters are listed in Table III. As shown in Table III, the R_a and R_q values of the pure iPP membrane, Ma, were 19.7 and 24.7, respectively, whereas the R_a and R_q values of the Me membrane were 39.2 and 54.6, respectively. The Ma membrane exhibited the smoothest surface, and the Me membrane exhibited the roughest surface. This result was consistent with the viewpoint reported by Cui *et al.*[28] The surface roughness of the modified blend membrane was apparently higher than that of the unmodified membrane. The higher roughness might have been related to the higher porosity of the external

Table II. Pore Parameters of the Prepared Membranes

Membrane	Porosity (%)	Mean pore size (μm)	Maximum pore size (μm)
Ma	35.45	0.36	0.77
Mb	46.83	0.24	0.50
Mc	59.75	0.13	0.29
Md	51.81	0.16	0.45
Me	40.13	0.33	0.69

The mean pore sizes of these PVDF-TiO_2 hybrid membranes were greater than 0.35 μm.[30] The mean pore size of the PVDF-SiO_2 hybrid membranes was 0.36 μm.[31]

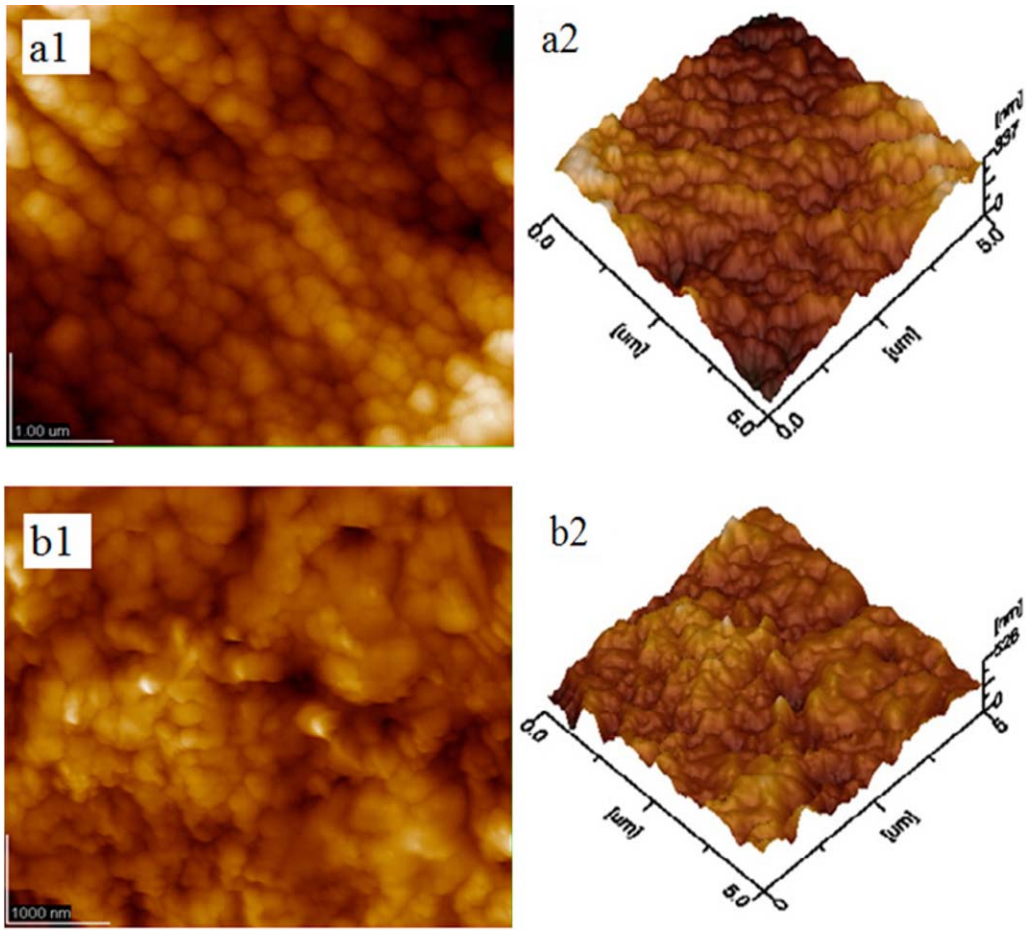

Figure 6. Two-dimensional and three-dimensional surface morphologies of the iPP/SiO_2 membranes: (a) Ma and (b) Me. [Color figure can be viewed in the online issue, which is available at wileyonlinelibrary.com.]

surface of membrane; this led to two changes in the composite membranes: one was an increase in the efficient MD area, and the other was an increase in the antifouling performance.

The CA of the membranes increased with the addition of hydrophobically modified nano-SiO_2. The membrane hydrophobicity increased with roughness because of contaminants accumulating in the valleys of the rough membrane surfaces.[29] The Me membrane exhibited the greatest hydrophobicity. Thus, the results indicate that the addition of nanoparticles could be a useful way to improve membrane hydrophobicity.[30]

EDS and XPS Analysis

Higher magnification field emission scanning electron microscopy (FESEM) and energy dispersive spectroscopy (EDS) analysis of the Mc membrane were carried out to identify the existence of SiO_2 nanoparticles in two different positions of the cross section, as shown in Figure 7.

The SiO_2 nanoparticles are shown with red frames in the FESEM images. There were Si and O in the EDS analysis. The existence of Au was due to the Au sputtering during the membrane pretreatment before FESEM.

In addition, in the process of membrane preparation, SiO_2 nanoparticles were dispersed homogeneously by an ultrasonic dispersion instrument. Then, the cast solution was stirred at 200°C for approximately 4 h to achieve a homogeneous mixture. Finally, the membrane was cooled and solidified by a water bath. After that, the pristine membranes were immersed in *n*-hexane for 24 h to completely remove the residual solvent. There was no other factor to disturb or to induce the distribution of SiO_2 nanoparticles after the ultrasonic dispersing process. This was evidence of the existence of the SiO_2 nanoparticles in the iPP/SiO_2 membrane.

The surfaces of the membranes from different dope solutions were characterized by XPS. With the Mc membrane as an example, the full spectrum in Figure 8 shows that the characteristic

Table III. Roughness Parameters and CA Values of the Membranes from Different Dope Solutions

Membrane	R_a (nm)	R_q (nm)	CA (°)
Ma	19.70	24.70	98.00 ± 0.30
Mb	23.40	27.70	105.48 ± 0.20
Mc	32.30	37.60	111.08 ± 0.30
Md	33.80	46.70	115.30 ± 0.50
Me	39.20	54.60	118.50 ± 0.70

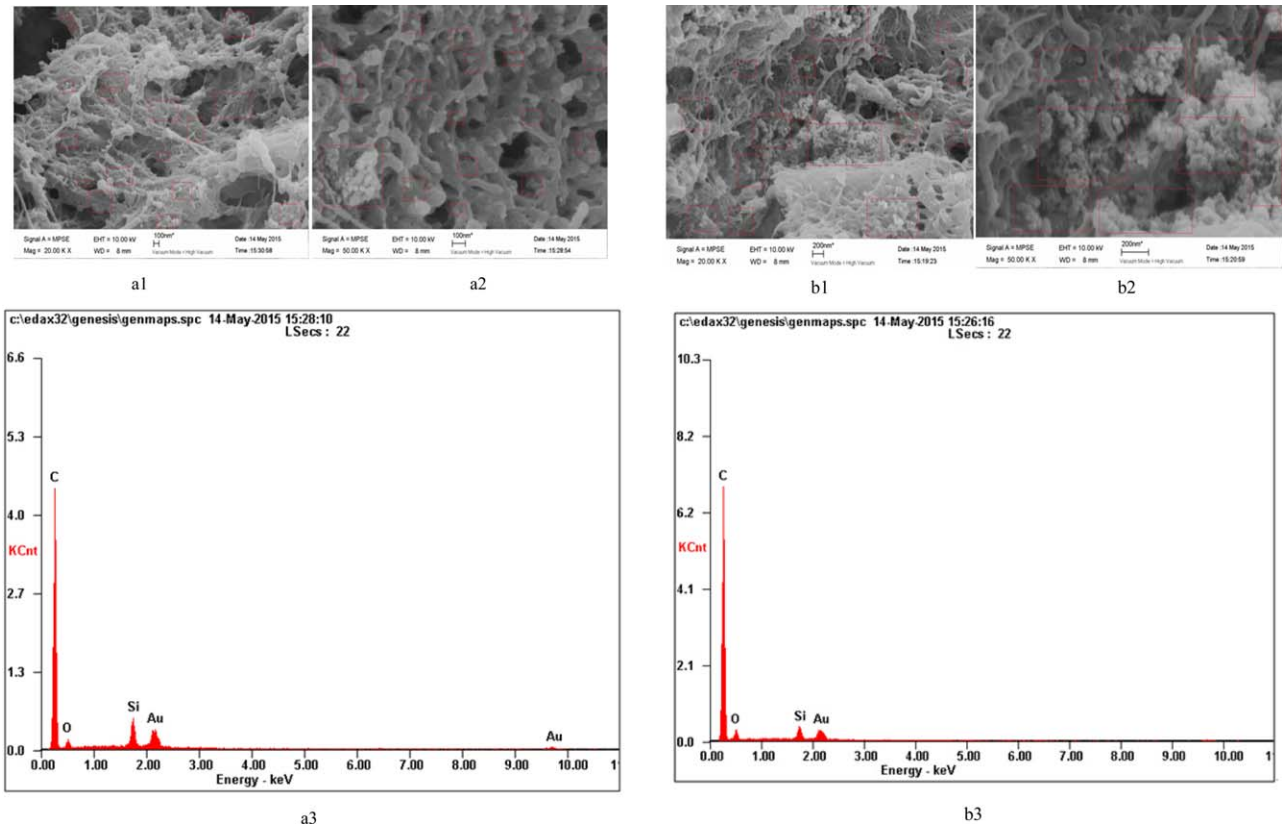

Figure 7. Cross-sectional FESEM image and EDS analysis of the Mc membrane (a1 and a2 are 20k and 50k magnification FESEM images in the first position, whereas, b1 and b2 are 20k and 50k magnification FESEM images in the second position, respectively. (a3 is EDS analysis of Mc membrane in the first position, whereas, b3 is EDS analysis of Mc membrane in the second position, respectively.) KCnt = 1000 X-ray counts. [Color figure can be viewed in the online issue, which is available at wileyonlinelibrary.com.]

peaks were C (1S) at 284.8 eV, Si (2p) at 103.8 eV, and O (1S) at 532.8 eV. The characteristic peak of Si (2p) indicated the existence of SiO_2 on the membrane surface. The molar fraction of a certain element can be obtained from the area fraction of the characteristic peak.

As shown in Table IV, the tested XPS data on the membrane surface were larger than the calculated data from the dope solutions; this provided evidence of nano-SiO_2 migration to the membrane surface.

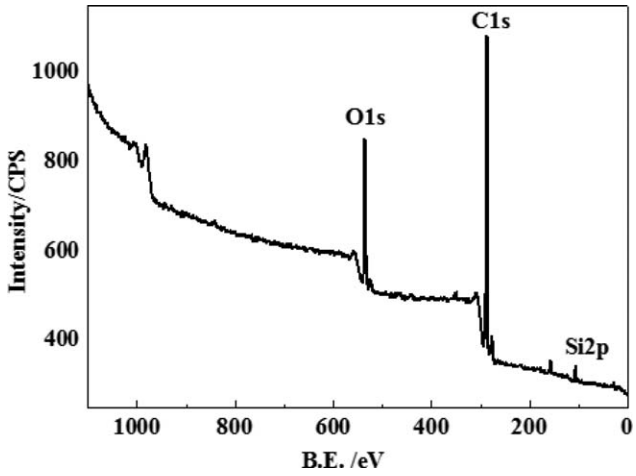

Figure 8. XPS spectra for the surface of the Mc membrane. CPS = X-ray photoelectron counts per second; BE = bind energy.

Membrane Antifouling Performances in the VMD Process

The fabricated membranes were applied to the concentration of the astragalus extract aqueous solution with the VMD process. In the VMD process, the feed temperature was 70°C, the feed flow rate was 50 L/h, and the vacuum degree was −0.095 MPa. During the long-duration running process, the flux declined. The flux decreased with time during the concentration process, as shown in Figure 9(a), and Figure 9(b) shows the rate of decline in the flux over time. The flux of the Mc membrane decreased from 12.64 to 3.01 kg m^{-2} h^{-1}; that is, the decline rate was 76.19%. The flux of the Ma membrane decreased from

Table IV. Si/C Molar Ratio

		n (Si)/n (C) (10^{-3})	
Membrane	SiO_2 (wt %)	XPS tested data	Calculated data
Mb	1	37.24	11.67
Mc	2	52.41	23.33
Md	3	96.62	35.00
Me	4	113.77	46.66

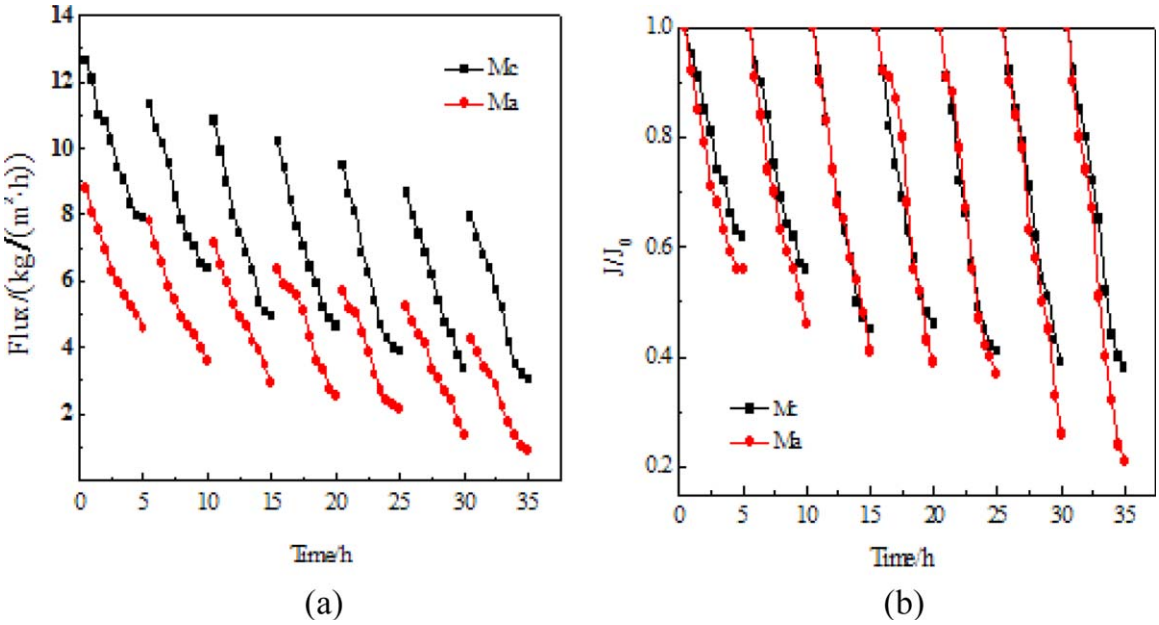

Figure 9. (a) Flux changes over time for membranes Ma and Mc, (b) Rate of flux decline over time for membranes Ma and Mc. J = instantaneous flux; J_0 = original flux. [Color figure can be viewed in the online issue, which is available at wileyonlinelibrary.com.]

8.81 to 0.90 kg m^{-2} h^{-1}; that is, the flux decline rate was 89.78%, which was much higher than that of Mc. The lower decline rate for Mc was attributed to the increase in the membrane hydrophobicity. During the concentrating process, the foulants were incessantly deposited onto the membrane surface (as shown in the SEM photograph). This deposition resulted in the growth of the fouling layer; therefore, its thermal resistance increased gradually, and this contributed to the observable

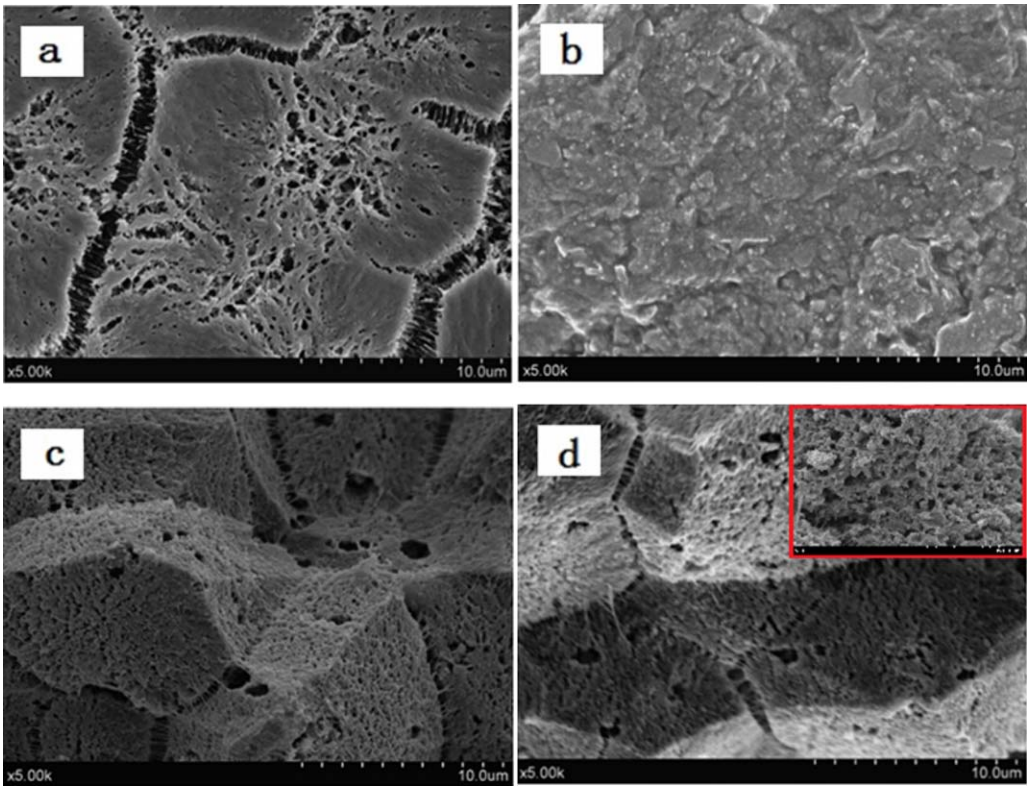

Figure 10. SEM images of membranes (a) Top surface image of the pristine membrane Ma, (b) top surface image of membrane Ma after MD for 5 h, (c) Cross-sectional image of the pristine membrane Ma, (d) Cross-sectional image of membrane Ma after MD for 5 h. (The magnification image of a part close to the fouled membrane surface is in the red frame.) [Color figure can be viewed in the online issue, which is available at wileyonlinelibrary.com.]

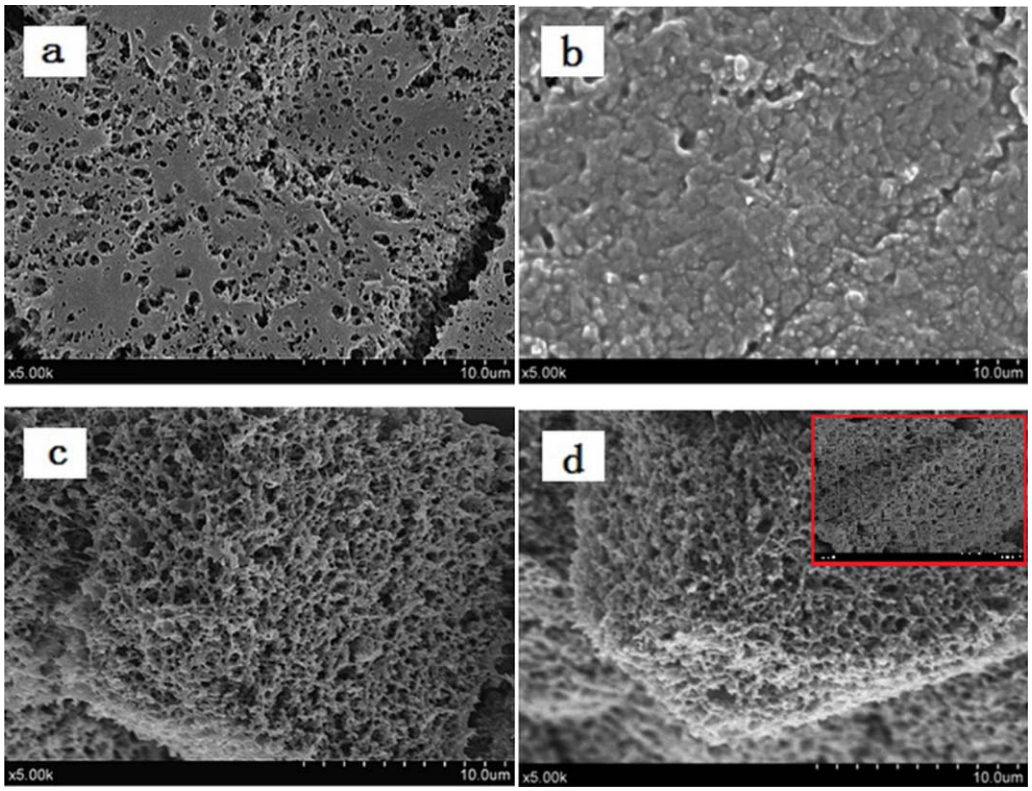

Figure 11. SEM images of membranes (a) Top surface image of the pristine membrane Mc, (b) top surface image of membrane Mc after MD for 5 h, (c) Cross-sectional image of the pristine membrane Mc, (d) Cross-sectional image of membrane Mc after MD for 5 h. (The magnification image of a part close to the fouled membrane surface is in the red frame.) [Color figure can be viewed in the online issue, which is available at wileyonlinelibrary.com.]

flux decline. The hydrophobicity of the Mc membrane ($111.08 \pm 0.30°$) was 13.35% greater than that of the Ma membrane ($98.00 \pm 0.30°$) because of the Lotus effect. When the feed solution flowed over the membrane surface, the hydrophobic nano-SiO_2 particles on the membrane surface prevented the astragalus extract aqueous solution from contacting the surface of the Mc membrane and adsorbing firmly onto it. Thus, the lower the amount of foulants absorbed onto the membrane surface was, the slower the rate of flux decline was. Therefore, the antifouling performance of the Mc membrane was improved via the introduction of hydrophobic nano-SiO_2 particles into the membranes.

During the VMD testing process, there were no astragalus polysaccharides detected on the permeate side; this indicated that η was 100%. As shown in Figures 10 and 11, we also observed that no foulants intruded into the membrane pores; this indicated that no membrane wetting occurred. Also, because the strong hydrophobicity of the membrane prevented liquid water from entering the membrane pores, there was no adsorption of foulants inside the wall of the membrane pores.

In the VMD experiment, the decline rate of Mc was consistent with that of Ma. The reason for this phenomenon might have been the high concentration of the astragalus aqueous solution. The main components of astragalus aqueous solution were 1–50 μm polysaccharose suspended particulates. The membrane surface was easily polluted by these polysaccharose particulates. A diluent of astragalus aqueous solution might have been an effective way to alleviate the membrane pollution. Therefore, the concentration factor of the solution might be an important parameter. In a future work, a diluted solution with different concentrations will be discussed.

CONCLUSIONS

In this study, iPP hydrophobic flat-sheet membranes were fabricated for use in MD through TIPS by the hydrophobic dispersion of modified SiO_2 nanoparticles in an iPP casting solution. The characterization of the membrane structure and VMD flux indicated that the addition of nano-SiO_2 enhanced the polymer crystallization temperature, acted as a nucleating agent, and influenced the membrane formation process; this resulted in different membrane structures. AFM studies revealed that the membrane surface roughness and CA increased with the addition of SiO_2 nanoparticles. With the addition of SiO_2, ε increased when the SiO_2/iPP ratio was below 10 : 100 and then decreased when the mixing ratio exceeded 10 : 100. This indicated that a certain amount of nanoparticles could enhance the permeability to some extent. Compared with the pure iPP membrane, the SiO_2/iPP membranes exhibited a stronger resistance to membrane fouling; this is a vital factor in their performance in the concentration of astragalus aqueous solution and for other desalination MD applications.

ACKNOWLEDGMENTS

The authors thank the National Nature Science Foundation (contract grant number 21376178), Tianjin Industry & Economic Development Area (TIDA) Giant Growth Plan (contract grant number 2011-XJR13020), Tianjin Science and Technology Support Program (contract grant number 12ZCDZSF06900), National Nature Science Foundation (contract grant number 12JCZDJC30000), Training Program for Changjiang Scholars and Innovative Research Team in University (contract grant number [2013]373), Innovative Research Team of Tianjin Municipal Education Commission (contract grant number TD12–5004), and College Students Innovation and Entrepreneurship Training Program (contract grant number 201410057075) for financial support.

REFERENCES

1. Lawson, K. W.; Lloyd, D. R. *J. Membr. Sci.* **1997**, *124*, 1.
2. Mengual, J. I.; Pena, L. *Colloid Interface Sci.***1997**, *1*, 17.
3. El-Bourawi, M. S.; Ding, Z.; Ma, R.; Khayet, M. *J. Membr. Sci.* **2006**, *285*, 4.
4. Alkhudhiri, A.; Darwish, N. *Desalination* **2012**, *287*, 2.
5. Sun, A. C.; Kosar, W.; Zhang, Y.; Feng, X. *J. Membr. Sci.* **2014**, *455*, 131.
6. Tian, R.; Gao, H.; Yang, X. H.; Yan, S. Y.; Li, S. *Desalination* **2014**, *332*, 52.
7. Khayet, M.; Cojocaru, C.; Baroudi, A. *Desalination* **2012**, *287*, 159.
8. Yang, Z. S.; Li, P. L.; Zhi, L. X.; Wang, S. C. *Desalination* **2006**, *192*, 168.
9. Tang, N.; Jia, Q.; Zhang, H. J.; Li, J. J.; Cao, S. *Desalination* **2010**, *256*, 27.
10. Rao, G.; Hiibel, S. R.; Achilli, A.; Childress, A. E. *Desalination* **2015**, *367*, 197.
11. Hou, D.; Wang, J.; Sun, X.; Ji, Z.; Luan, K. *J. Membr. Sci.* **2012**, *405*, 185.
12. Gryta, M. *J. Membr. Sci.* **2005**, *265*, 153.
13. Mohammadi, T.; Madaeni, S. S.; Moghadam, M. K. *Desalination* **2002**, *153*, 155.
14. Alklaibi, A. M.; Lior, N. *Desalination* **2005**, *171*, 111.
15. Lv, Y. X.; Yu, X. H.; Tu, S. T.; Yan, J. Y.; Dahlquist, E. *J. Membr. Sci.* **2010**, *362*, 444.
16. Prince, J. A.; Singh, G.; Rana, D.; Matsuura, T.; Anbharasi, V.; Shanmugasundaram, T. S. *J. Membr. Sci.* **2012**, *397–398*, 80.
17. Suk, D. E.; Matsuura, T.; Park, H. B.; Lee, Y. M. *Desalination* **2010**, *261*, 300.
18. Hou, D.; Wang, J.; Qu, D.; Luan, Z.; Ren, J. *Sep. Purif. Technol.* **2009**, *69*, 78.
19. Gu, M. H.; Wang, J.; Wang, X. L. *Desalination* **2006**, *192*, 160.
20. Lloyd, D. R.; Barlow, J. W.; Kinzer, K. E. *AIChE Symp. Ser.* **1988**, *74*, 28.
21. Hiatt, W. C.; Vitzthum, W. C. In Materials Science of Synthetic Membranes; ACS Symposium Series 269; Lloyd, D. R., Ed.; American Chemical Society: Washington, DC, **1985**.
22. Xu, Y.; Zheng, W. T.; Yu, W. X.; Hua, L. G.; Zhang, Y. J.; Zhao, Z. D. *Chem. Res. Chin. Univ.* **2010**, *25*, 491.
23. Khayet, M.; Khulbe, K. C.; Matsuura, T. *J. Membr. Sci.* **2004**, *238*, 199.
24. Ding, Z. W.; Liu, L. Y.; Yu, J. F.; Ma, R. Y.; Yang, Z. R. *J. Membr. Sci.* **2008**, *310*, 539.
25. Matsuyama, H.; Maki, T.; Teramoto, M. *J. Membr. Sci.* **2002**, *204*, 323.
26. Amir, R.; Ellen, A.; Guangxi, D.; Jaleh, M.; Vicki, C. *J. Membr. Sci.* **2012**, *415–416*, 850.
27. Jing, Z.; Zhenyu, S.; Baoan, L.; Qin, W.; Shichang, W. *Desalination* **2013**, *324*, 1.
28. Cui, A.; Liu, Z.; Xiao, C.; Zhang, Y. *J. Membr. Sci.* **2010**, *360*, 259.
29. Liu, Y.; Yu, S. L.; Chai, B. X.; Shun, X. *J. Membr. Sci.* **2006**, *276*, 162.
30. Deyin, H.; Jun, W.; Xiangcheng, S.; Zhongguang, J.; Zhaokun, L. *J. Membr. Sci.* **2012**, *405*, 185.